Available online at www.sciencedirect.com
SCIENCE DIRECT®
Journal of Solid State Chemistry 177 (2004) 856–865
JOURNAL OF SOLID STATE CHEMISTRY
http://elsevier.com/locate/jssc

Effects of temperature and Nd composition on non-linear transport properties in substituted $Ce_{1-x}Nd_xO_{2-\delta}$ cerium dioxides

Latifa Aneflous,[a] Jean A. Musso,[b] Sylvie Villain,[b] Jean-Raymond Gavarri,[b,*] and Houria Benyaich[a]

[a] *Faculté des Sciences, Laboratoire de chimie du solide, Université Ibn Zohr, BP 28/S, 80 000, Agadir, Maroc, Morocco*
[b] *Laboratoire des Matériaux & Microélectronique de Provence (UMR CNRS 6137), Multiphases et Interfaces, Université de Toulon-Var, BP 132, 83957 La Garde, Cedex, France*

Received 16 June 2003; received in revised form 15 September 2003; accepted 22 September 2003

Abstract

Cerium dioxides doped or substituted by neodymium have been prepared using low- (320°C) and high-temperature (1600°C) processes. The Nd substituted ceria phase obtained at high temperature is a solid solution $Ce_{1-x}Nd_xO_{2-\delta}$ $0 \leqslant x \leqslant 0.30$. Electrical impedance spectroscopy analyses have been performed in the temperature range 40–700°C. At temperatures above 400°C, Nyquist representations allow to separate three signals corresponding to bulk, grain boundary and electrode responses. Non-linear variations of the resistance and the capacitance as functions of temperature and composition x are observed. In the case of grain boundary and electrode interface signals, constant phase elements with non-integer exponent n have been used to represent the equivalent circuits. For each contribution, the conductance strongly increases then reaches a limit value, above $x = 0.10$. When composition x increases, the condensation of Nd-vacancy defect clusters might be at the origin of the non-linear evolution of the conductance. Bulk and grain boundary conductions present different activation energies (0.7 and 1.3 eV).

Keywords: Neodymium cerium dioxides; Impedance spectroscopy; Conductivity; Capacitance; Constant phase element; Heterogeneous ceramics

1. Introduction

For many years CeO_2-based materials have been intensively investigated as catalysts, structural and electronic promoters of heterogeneous catalytic reactions and oxide-ion conducting solid electrolytes in electrochemical cells [1–3]. For this last application, relatively high ionic conductivity of the solid electrolyte is required for device performance. The oxygen vacancy $[V_O^{\bullet\bullet}]$ concentration and the conductivity in cerium oxide can be increased by the substitution of cerium (+IV) by metal ions having a lower valency [4–6]. In this case, the chemical formula can be expressed as follows: $Ce_{1-x}^{4v+}M_x^{3+}O_{2-x/2}\,[V_O^{\bullet\bullet}]_{x/2}$ where $[V_O^{\bullet\bullet}]$ designates an oxygen vacancy, considered as a doubly positively charged vacancy. In such fluorite-type structures, two cationic defects M^{3+} (noted as being a negatively charged defect M'_{Ce}) might be more or less linked to one vacancy. Inaba [1] showed that $\{M'_{Ce}-[V_O^{\bullet\bullet}]-M'_{Ce}\}$ extended defects (or clusters) might be formed at low temperature and could dissociate at higher temperatures. It should be noted that, as the presence of vacancies increase oxygen mobility, these mobile species should also actively participate in surface interactions with adsorbed molecules. As catalytic and conduction behaviors are correlated through defect structure, it should be interesting to better understand the various conduction mechanisms in ceria and to distinguish surface and bulk behaviors.

Many authors extensively studied the electrical conduction mechanisms in substituted ceria $Ce_{1-x}M_xO_{2-y}$; however, a large dispersion of results can be observed as well as for conductivity or for activation energies.

In the case of Ca doped ceria [7], the ionic conduction was found to present a wide maximum for a molar fraction of 8 Ca at%, with a decrease of conduction from 13 Ca at%. Generally, the activation energy of electrical conduction was found to range between 0.6 and 1 eV.

*Corresponding author. Fax: +33-494-142311.
E-mail address: gavarri.jr@univ-tln.fr (J.-R. Gavarri).

0022-4596/$ - see front matter © 2003 Elsevier Inc. All rights reserved.
doi:10.1016/j.jssc.2003.09.020

For lanthanide doping (Y_2O_3, La_2O_3 to Yb_2O_3), several authors [8–10] reported similar electrical behaviors.

To date, the composition dependence of activation energy is not clearly established: for some authors [8,9], activation energy and cell parameter both vary with composition, while for Dirstine et al. [10], activation energy should be constant. For Hohnke [11], below a certain fraction of doping element, the activation energy of conduction should vary, while, above this fraction, the conduction should be independent of doping fraction.

In the case of the series $(CeO_2)_{0.8}(Ln_2O_3)_{0.2}$ (Ln = La, Nd, Sm, Eu, Gd, Y, Ho, Tm, Yb) at 800°C, Yahiro et al. [12] reported conductivity values that depended on the nature of doping element. However, the effective values reported in these works were generally dispersed; it should be noted that the same authors reported contradictory results [13]. To interpret such a dispersion in experimental results, it was invoked that grain boundaries probably could play a prominent role in the resulting electrical data.

Riess et al. [14] clearly demonstrated that the ionic conductivity of the system $(CeO_2)_{0.82}(Gd_2O_3)_{0.18}$ strongly depended on the preparation routes of ceramics.

From electrical impedance analyses, Wang et al. [15] showed that the contributions of grain boundaries and of the bulk (grain core) to the conduction could be separated; the electrical resistance of grain boundaries was found to be greater than that of the grain core. This fact was ascribed to the presence of amorphous insulating phases in these boundaries. As grain boundaries are strongly conditioned by preparation process and thermal treatment, the total conduction necessarily strongly depends on the preparation process. These authors also showed that the activation energies of intra-grain conduction should strongly vary with the doping fraction.

Faber et al. [16] showed that, for the Yb, Y, Gd, La and Nd series, it should be expected that activation energy could present a minimum as a function of doping fraction. This evolution should be associated with progressive ordering of defects as the doping fraction increases.

In the case of the specific composition $Ce_{0.9}Gd_{0.1}O_{1.95}$, Huang et al. [17] proposed that, in a certain temperature range of ± 45°C below and above $T = 583$°C, mobile vacancies should condense and activation energy should be fixed at 0.63 eV.

Kilner et al. [18] established correlations between ionic radii and defect formation in the lattice: the ionic conduction should be directly connected with ionic sizes or cell parameters.

In this work, we first synthesize multiphase neodymium doped ceria at low temperature, and then we elaborate and characterize the solid solutions. Finally, we try to better understand the role of Nd doping and of working temperature in electrical transport properties.

2. Experimental

Nanosized powders of CeO_{2-z} ceria were first synthesized with a sol–gel method, previously described in our study [19] and using mono-hydrate cerium (+III) oxalate ($Ce_2(C_2O_4)_3 \cdot 9H_2O$, 99.9% Strem chemicals) mixed in absolute ethanol.

Then, samples of $x NdO_{1.5}-(1-x)CeO_{2-\delta}$ ($0 \leqslant x \leqslant 0.30$) were synthesized by the same sol–gel method using appropriate proportions of mono-hydrate neodymium(+III) acetate ($Nd(CH_3COO)_3 \cdot H_2O$, 99.9% Strem chemicals), mixed in absolute ethanol. The solution was stirred for 1 h and then treated at 65°C until a gel was formed. The obtained gel was then thermally treated at 320°C for 2 h.

A first hypothetical intermediate reaction can be assumed for the preparation process as follows:

$$\begin{aligned}&\{(1-x)Ce_2(C_2O_4)_3 \cdot 9H_2O \\ &\quad + 2xNd(CH_3COO)_3 \cdot H_2O\} + mO_2(\text{air}) \\ &\rightarrow 2(1-x)CeO_{2-z} + xNd_2O_3 + p \cdot H_2O \\ &\quad + qCO + q'CO_2,\end{aligned}$$

where p, q and q' are directly connected with the x atom fraction and with the effective m values (oxygen) close to the reactants.

From thermal analyses, it was established that the decomposition of the precursors is generally associated with a first dehydration (lattice water departure), then a first decomposition step giving CO and CO_2 gas emissions (with additional water), and finally formation of the solid phases. This intermediate local atmosphere is more or less reductive and depends on the kinetic conditions of decomposition: this should modify the ceria non-stoichiometry (in the formula CeO_{2-z}, z depends on reduction step and on kinetics).

Finally, to form solid solutions with the resulting chemical formula $Ce^{4+}_{1-x}Nd^{3+}_{x}O_{2-x/2}$, additional sintering processes at high temperature have to be performed, at sufficiently high temperatures.

The Nd-doped CeO_2 nano-powders were then ground and pressed at 5 kbar into pellets, using a stainless steel die with 13 mm diameter. Densities of the pellets were measured using the Archimede's method with water, and were related to the theoretical values determined from cubic lattice parameters. The measured densities of the samples are about 60% of the theoretical ones.

The pellets were then sintered, with a programmed heating and cooling rate of 3°C/min, at 1600°C, for 10 h, in order to obtain a solid solution. The sintered samples presented an experimental density of about 85% of the

theoretical one. The final dimensions were determined for each sample. Dimensions of pellets were quasi-constant with diameters close to 13 mm and thickness of about 1.5 mm.

Phase identifications, lattice parameter determinations, and then crystallite size evaluations were performed, using X-ray diffraction (XRD) analyses. The XRD patterns were collected, using a Siemens–Brucker D5000 diffractometer, equipped with a copper X-ray source ($\lambda_{K\alpha1} = 1.54056$ Å, $\lambda_{K\alpha2} = 1.54493$ Å), a secondary monochromator (to withdraw the K_β-ray) and a rotating sample holder, working in a classical coupled $\theta-2\theta$ mode.

Scanning electron microscopy (SEM) analyses were carried out using a PHILIPS XL30 equipment to characterize the morphology and the distribution of the phases in the synthesized nano- and micropowders. The local composition of each phase was determined making use of EDAX analysis.

The conductivity was determined under air, in the temperature range 40–700°C. The equipment was a Solartron SI 1260 AC impedance analyzer. The frequencies ranged from 0.1 Hz to 10 MHz. For a given temperature, each measurement was carried out after a preliminary heating time of 15 min.

3. Results and discussion

3.1. Characterization of the nanopowders

The interest of the sol–gel method resides in the fact that, generally, the resulting multiphase powders can present small grain sizes allowing lowering the sintering temperatures. In the present case, as nano-sized ceria particles and crystalline phase Nd_2O_3 coexist reactivity is increased, which might allow easier formation of solid solutions at lowered temperatures. The mean ceria grain sizes were determined from XRD profile analyses Fig. 1.

The results of XRD analyses show that all of ours samples ($0 \leqslant x \leqslant 0.30$) are formed with a fluorite fcc structure. The average crystallite size D of the sol–gel prepared powders was calculated using the Scherrer formula:

$$D = 0.9\lambda/\beta\cos\theta, \quad (1)$$

where λ is the wavelength of the X-ray, θ is the diffraction angle associated with a Bragg peak, $\beta = (\beta_m^2 - \beta_s^2)^{1/2}$ is the corrected half-width at half-maximum (HWHM), β_m being the total HWHM of the Bragg peak, β_s being that of a standard crystallized sample of CeO_2. Calculated peak profiles were fitted to the experimental data, using mathematical functions (WinPlotter program [20]). This allowed us to determine the position and the integrated peak widths with a good accuracy. The (*hkl*) Bragg peaks used to refine the various parameters were: (111), (200), (220), (311), (222), (400), (331), (420), (422) and (511).

The calculated values of the ceria crystallite sizes range between 4.3 and 5.8 nm (Table 1). It should be remarked that this particle size clearly increases with the rate of Nd doping element. As the Nd content increases, the cell parameter surprisingly slowly decreases (line a in Fig. 2). This evolution might have two origins: first, it might be due to the variation of diffraction profiles as the Nd content increases, secondly, it might be involved by oxygen non-stoichiometry resulting from the reductive atmosphere of preparation process. A similar effect of preparation conditions was observed in our recent work [19].

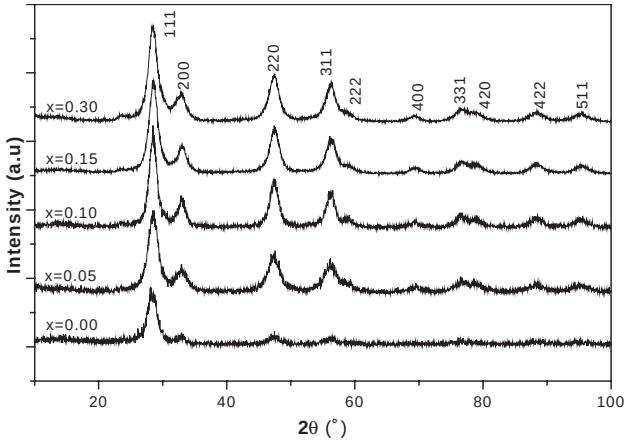

Fig. 1. Powder XRD patterns of $xNdO_{1.5}$–$(1-x)$ $CeO_{2-\delta}$ ($0 \leqslant x \leqslant 0.30$) prepared at 320°C by sol–gel process.

Table 1
Crystallite size and cell parameter of ceria phase, in the case of multiphase system $xNdO_{1.5}$–$(1-x)CeO_2$ ($0 \leqslant x \leqslant 0.30$), synthesized by sol–gel at 320°C

Component	D (nm)	a (pm)	σ_a (pm)	$V \times 10^{-6}$ (pm^3)	$\sigma_V \times 10^{-5}$ (pm^3)
CeO_2	4.3	541.57	0.2	158.8	2
$(CeO_{2-\delta})_{0.95}(NdO_{1.5})_{0.05}$	4.8	541.64	0.4	158.9	4
$(CeO_{2-\delta})_{0.90}(NdO_{1.5})_{0.10}$	4.6	541.47	0.2	158.7	2
$(CeO_{2-\delta})_{0.90}(NdO_{1.5})_{0.15}$	4.9	541.10	0.4	158.4	4
$(CeO_{2-\delta})_{0.80}(NdO_{1.5})_{0.20}$	5.8	541.10	0.4	158.4	4
$(CeO_{2-\delta})_{0.75}(NdO_{1.5})_{0.25}$	5.3	541.14	0.4	158.4	4
$(CeO_{2-\delta})_{0.70}(NdO_{1.5})_{0.30}$	5.8	540.94	0.6	158.2	5

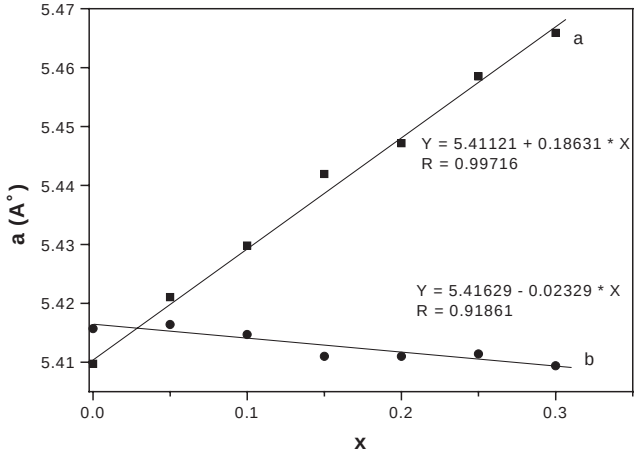

Fig. 2. Cell parameter vs. x: (a) sintering temperature $T = 1600°C$; and (b) sol–gel at 320°C.

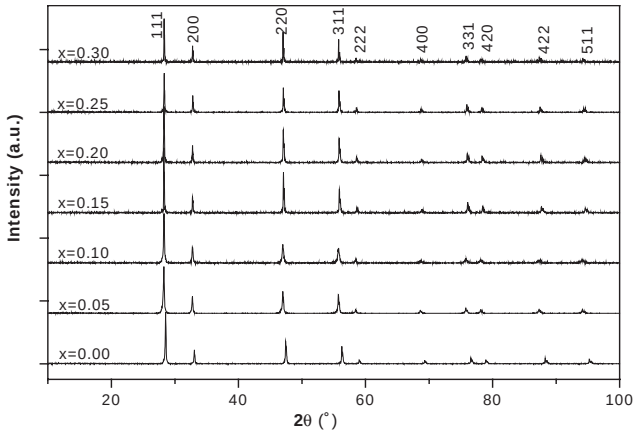

Fig. 4. Powder XRD patterns of $Ce_{1-x}Nd_xO_{2-\delta}$ ($0 \leqslant x \leqslant 0.30$) sintered at 1600°C.

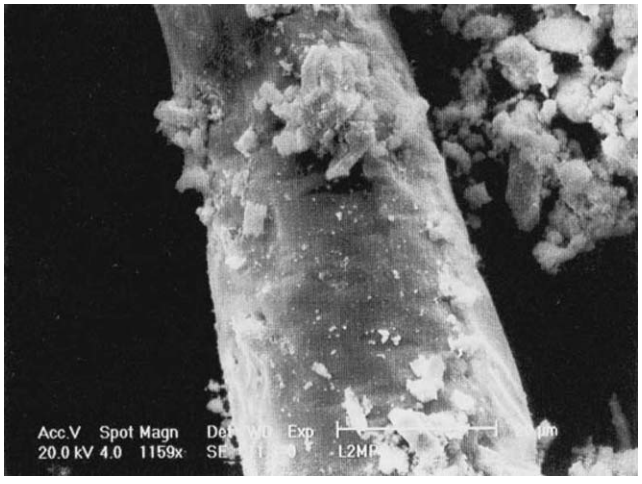

Fig. 3. SEM image of $(CeO_{2-\Delta})_{0.85}(NdO_{1.5})_{0.15}$ prepared by sol–gel at 320°C.

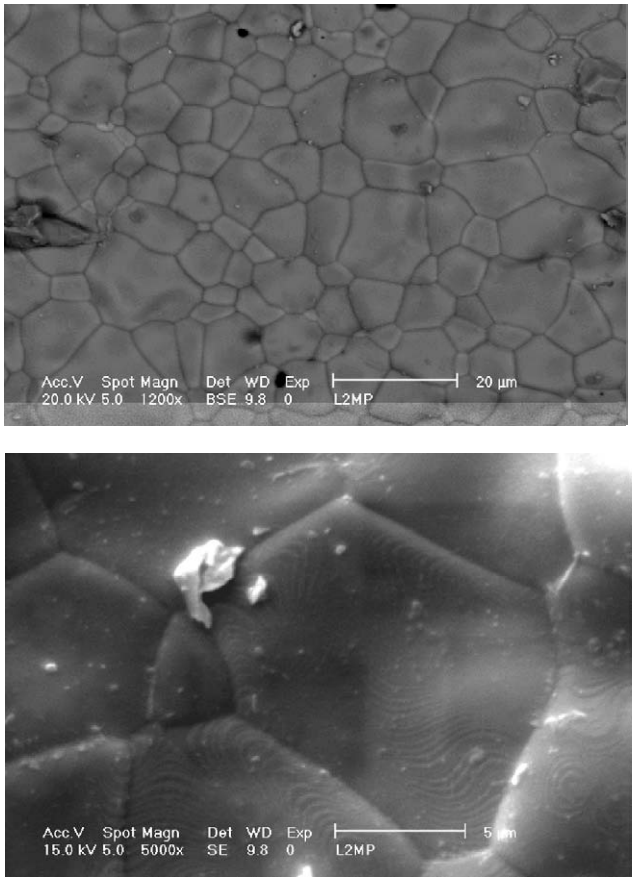

Fig. 5. SEM micrograph of $Ce_{0.75}$ $Nd_{0.25}O_{2-\delta}$ sintered at 1600°C.

SEM measurements were performed to observe the morphology and determine grain sizes (Fig 3). Two particle shapes were observed in the samples. The X-ray emission (EDAX) analysis of small particles (1 µm), having a regular geometric form, confirmed the CeO_2 composition. Thick particles, which appear like sticks, had a high Nd content. No trace of carbon was found.

3.2. Characterization of the micropowders

In order to obtain a solid solution, the samples elaborated by sol–gel were then sintered at 1600°C, under air, for 10 h, with a programmed heating and cooling rate of 3°C/min. XRD measurements showed that the initial ceria fluorite lattice is conserved. No Nd_2O_3 crystalline phase is observed (Fig. 4). Dependence of lattice parameter vs. doping concentration of Nd^{3+} is shown in Fig. 2 (line b). As the Nd composition increases, the experimental lattice parameter a (expressed in pm) linearly increases as:

$$a(x) = 541.12 + 18.63x \quad (2)$$

for $Ce_{1-x}Nd_xO_{2-x/2}$ ($0 \leqslant x \leqslant 0.25$), which is in quite good agreement with a classical solid solution obeying the Vegard's rule. This result is in good agreement with

the effective ionic radii for eight-fold coordinated Ce^{4+} ($r^{4+}_{Ce} = 97.0$ pm) and Nd^{3+} ions ($r^{3+}_{Nd} = 110.9$ pm) [21].

Fig. 5 shows a typical microstructure for $Ce_{0.75}Nd_{0.25}O_{2-\delta}$ ceramics sintered at 1600°C, under air, for 10 h. Grain sizes typically vary between 5 and 17 μm. The grain size distribution is very uniform. Grain boundaries are clearly visible. The composition of the samples, obtained from EDAX analyses, agrees with the nominal composition.

3.3. Electrical impedance spectroscopy

3.3.1. Measurements and electric signal treatments

To well characterize the oxygen or electron mobility in such materials, the obtained solid solutions $Ce_{1-x}Nd_xO_{2-\delta}$ ($0 \leqslant x \leqslant 0.25$), prepared at 1600°C, where analyzed by electrical impedance spectrometry as a function of composition x and temperature, in a wide frequency range (10^{-1}–10^{7} Hz). To interpret the electrical impedance analyses, Nyquist representations were systematically used: in such representations, the complex impedances $Z = Z' + jZ''$ are reported in a complex plane with $x = Z'$ and $y = -Z''$. Then, it is possible to choose well-adapted equivalent electrical circuits to fit the apparent successive semicircles observed in the complex plane [22].

Generally, a high-frequency semicircle originates in bulk conduction and dielectric processes. A low-frequency semicircle or arc is generally due to ion and electron transfers at the sample surface contacting the electrode. Finally, an intermediate-frequency semicircle provides information on the grain-boundary and/or impurity-phase contribution to ionic conduction.

In fact, to determine the electrical characteristics of the effective equivalent circuits associated with the observed Nyquist signals (high, medium and low frequencies), we have used the modified $R-C$ parallel circuits taking into account the fractal character of our heterogeneous porous systems [23,24], the so-called constant phase elements (CPE):

$$1/Z_i = 1/R_i + [jC_i\omega]^{n_i}. \quad (3)$$

In this expression, the R_i and C_i parameters designate the two classical resistance and capacitance of the ideal "Debye" circuit, and the exponent n_i describes the fractal character (the heterogeneous or porous character) of the sample.

Generally, at least three sets of (R_i, C_i and n_i) parameters are needed to describe the conduction behavior of bulk, interfaces and electrodes.

3.3.2. Temperature dependence of electrical parameters

The electric impedance spectra were fitted after optimizing the three sets of (R_i, C_i and n_i) parameters for bulk, grain boundary and electrode conductions making use of various equivalent circuits [25].

In Table 2a and Fig 6a, we have gathered all electrical characteristics of the bulk system, with R_i and C_i values of the RC model used to interpret the Nyquist representations.

In Table 2b and Fig. 6b, we have gathered all electrical characteristics of the grain boundary, in Tables 2c,d and Fig. 6c, we have gathered all electrical characteristics of the electrode processes, with R_i, C_i and n_i values of the CPE models used to interpret the Nyquist representations.

Impedance spectra in Nyquist representation show variable electrical behaviors depending on temperature range.

- In the low-temperature range (40–400°C), the bulk and grain boundary conductions are not separated in the Nyquist representation. In this case, one obtains the unique value of the total resistance or corresponding conductivity; however, the temperature dependence of total conductivity clearly shows significant deviations from a unique Arrhenius law (Fig. 7).
- In the high-temperature range (400–700°C), several impedance spectra (Nyquist arcs or circles) are observed (Fig. 8). These various contributions can be ascribed to the various conduction processes occurring in the bulk (highest frequencies ω), grain boundaries (intermediate ω), and electrode interfaces (low frequencies) and are based on different resistances and capacitances R and C in the equivalent parallel RC circuits.

3.3.3. Composition dependency of electrical parameters

It can be noted that, in the 40–260°C temperature range, the total conductivity is very weak and drastically increases with the doping fraction (Fig. 9), up to a composition $x = 0.15$. In this temperature range, a unique Nyquist circle is observed, and the various contributions cannot be separated.

In the case of high-temperature experiments (400–700°C), the various contributions can be separated, and non-linear evolutions are systematically observed, as in the low-temperature range.

The evolutions of the conductivity vs. composition x can be summarized as follows:

- *Bulk conduction*: a non-linear variation of $\log \sigma$ vs. the Nd composition x is observed with a quasi-constant value of σ above $x = 0.10$;
- *Grain boundary conduction*: we also observe a regular increase in σ followed by a quasi-constant value of σ above $x = 0.10$;
- *Electrode interface conduction*: non-linear variations are also observed, even if they are attenuated.

Table 2
Electrical characteristics

(a) for bulk: R_i, and C_i values of the RC model for $Ce_{1-x}Nd_xO_{2-\delta}$ $0 \leqslant x \leqslant 0.25$

t (°C)	$x = 0$		$X = 0.05$		$x = 0.10$		$x = 0.15$		$x = 0.20$		$x = 0.25$	
	R (kΩ)	C (pF)	R (kΩ)	C (pF)	R (kΩ)	C (pF)	R (kΩ)	C (pF)	R (kΩ)	C (pF)	R (kΩ)	C (pF)
400	345	36	11.4	20	6.8	12	7.4	26	8.4	26	6.4	26
420	242	37	8.2	20	4.9	13	5.4	27	5.6	27	4.3	28
440	158	38	5.8	21	3.6	15	3.7	29	4.2	29	3.1	30
460	102	38	4.4	22	2.6	18	2.6	31	3.0	30	2.2	33
480	67.3	37	3.4	23	1.9	23	1.9	33	2.2	33	1.5	37
500	43.2	36	2.6	25	1.4	31	1.4	39	1.6	36	1.1	42
540	18.7	34	1.6	33	0.7	63	0.7	53	0.8	48	0.6	63
580	8.8	31	1.0	57	0.4	145	0.3	132	0.3	93	0.5	61
600	6.2	35	0.8	73	0.3	208			0.2	184	0.3	115
640	3.3	30			0.1	467						
680	1.7	35										
700	1.3	35										

(b) for grain boundary: R_i, C_i and n_i values of the CPE models for $Ce_{1-x}Nd_xO_{2-\delta}$ $0.05 \leqslant x \leqslant 0.20$

t (°C)	$x = 0.05$			$x = 0.10$			$x = 0.15$			$x = 0.20$		
	R (kΩ)	C (10^6 pF)	n	R (kΩ)	C (10^6 pF)	n	R (kΩ)	C (10^6 pF)	n	R (kΩ)	C (10^6 pF)	n
400	367	0.04	0.59	213	1.09	0.37	295	0.63	0.42			
420	177	0.05	0.57	134	1.70	0.35	118	0.45	0.47	0.9	2.55	0.31
440	107	0.09	0.54	59	1.72	0.37	69	0.51	0.47	46	0.76	0.44
460	50.2	0.10	0.54	30	1.88	0.39	38	0.48	0.50	24	0.54	0.49
480	29.7	0.14	0.53	15	1.79	0.41	27	0.69	0.48	14	0.50	0.51
500	18.1	0.18	0.52	8.4	1.57	0.43	14	0.55	0.52	9	0.56	0.52
540	8.0	0.29	0.51	3.7	2.49	0.42	6	1.16	0.49	5	1.69	0.46
580	4.4	1.22	0.42	1.9	4.16	0.39	3	2.88	0.45	2.4	2.55	0.46
600	2.8	0.92	0.43	1.2	4.53	0.39	1	0.79	0.59	1.6	2.52	0.48
640	1.1	0.32	0.52	0.4	0.72	0.54	0.2	0.13	0.74	0.4	0.55	0.61
680	0.4	0.02	0.73	0.1	0.11	0.71	0.1	0.03	0.87	0.1	0.05	0.83
700	0.2	0.02	0.76	0.1	0.03	0.83	0.05	0.02	0.94	0.1	0.02	0.93

(c) for electrode processes: R_i, C_i and n_i values of the CPE models for $Ce_{1-x}Nd_xO_{2-\delta}$ $0 \leqslant x \leqslant 0.10$

t (°C)	$x = 0$			$X = 0.05$			$x = 0.10$		
	R (kΩ)	C (10^6 pF)	n	R (kΩ)	C (10^6 pF)	n	R (kΩ)	C (10^6 pF)	n
400							5410	0.49	0.58
420				7610	0.29	0.44	3441	0.62	0.57
440				4111	0.40	0.45	2343	0.79	0.56
460	552	1.60	0.26	2335	0.58	0.46	1350	0.94	0.57
480	381	1.85	0.3	1252	0.81	0.46	907	1.18	0.57
500	303	2.40	0.31	755	1.12	0.47	625	1.48	0.56
540	139	3.72	0.35	293	1.26	0.54	262	1.98	0.58
580	57	5.75	0.39	149	1.42	0.59	122	2.68	0.60
600	37	7.18	0.40	100	1.46	0.63	95	3.76	0.56
640	16	11.3	0.42	48	2.24	0.64	41	5.02	0.58
680	6	16.4	0.45	25	4.03	0.63	17	5.97	0.63
700	4	21.8	0.45	17	5.44	0.62	12	7.03	0.63

(d) for electrode processes: R_i, C_i and n_i values of the CPE models for $Ce_{1-x}Nd_xO_{2-\delta}$ $0.15 \leqslant x \leqslant 0.25$

t (°C)	$x = 0.15$			$x = 0.20$			$x = 0.25$		
	R (kΩ)	C (10^6 pF)	n	R (kΩ)	C (10^6 pF)	n	R (kΩ)	C (10^6 pF)	n
400	1230	0.92	0.48	792	0.85	0.50	9	2.06	0.46
420	1610	1.39	0.40	547	1.12	0.51	70	2.61	0.46
440	9780	1.67	0.41	457	1.50	0.49	487	3.18	0.47
460	7160	2.08	0.42	373	2.14	0.46	332	3.76	0.48
480	436	2.27	0.44	277	2.99	0.45	252	4.59	0.48
500	291	2.30	0.48	200	4.30	0.43	181	5.35	0.48
540	165	2.17	0.54	85	8.25	0.42	90	6.63	0.51

Table 2 (*continued*)

(d) for electrode processes: R_i, C_i and n_i values of the CPE models for $Ce_{1-x}Nd_xO_{2-\delta}$ $0.15 \leqslant x \leqslant 0.25$

t (°C)	$x = 0.15$			$x = 0.20$			$x = 0.25$		
	R (kΩ)	C (10^6 pF)	n	R (kΩ)	C (10^6 pF)	n	R (kΩ)	C (10^6 pF)	n
580	99	2.71	0.56	53	8.55	0.48	92	6.82	0.51
600	58	4.64	0.57	47	10.4	0.48	46	8.12	0.54
640	28	5.97	0.59	25	14.3	0.48	33	9.01	0.54
680	13	7.69	0.61	12	19.9	0.49	17	10.15	0.57
700	9	8.85	0.62	8	22.9	0.50	8	12.39	0.56

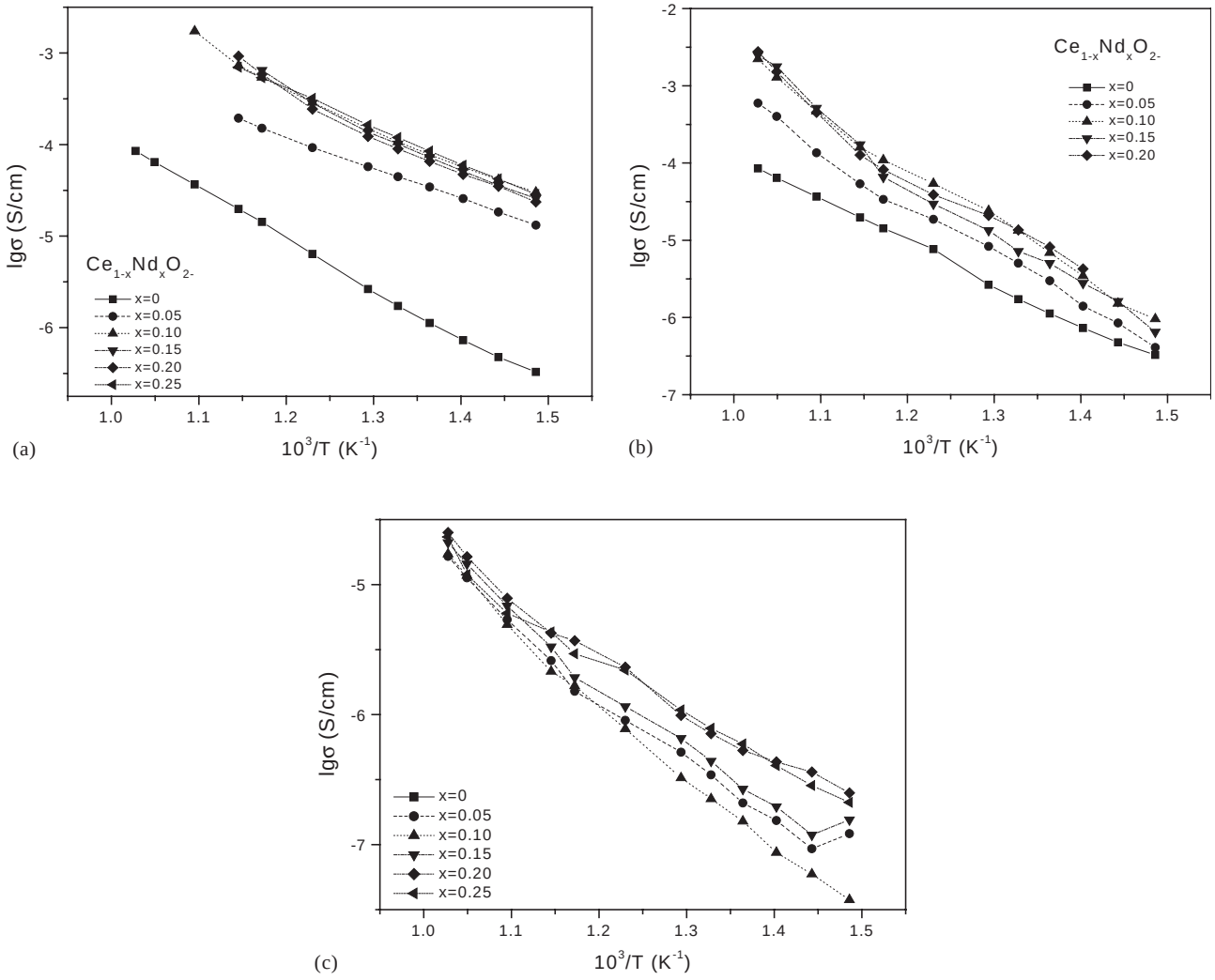

Fig. 6. (a) Bulk conductivity obtained for $Ce_{1-x}Nd_xO_{2-\delta}$ solid solutions, sintered at 1600°C; (b) grain boundary conductivity obtained for $Ce_{1-x}Nd_xO_{2-\delta}$ solid solutions, sintered at 1600°C; and (c) electrode conductivity obtained for $Ce_{1-x}Nd_xO_{2-\delta}$ solid solutions, sintered at 1600°C.

The activation energy values calculated from the Arrhenius plots for high ($t > 400$°C) and low temperatures are listed in Table 3

$$\sigma = \sigma_0 \exp(-E_a/k_B T). \quad (4)$$

In the low-temperature range, the activation energy is weak (0.04–0.22 eV with a relative error of 20%) and does not clearly depend on Nd atomic fraction [26,27]: it can be associated with extrinsic surface defect migration (including surface water and adsorbed gases).

In the high-temperature range, where defect clusters can dissociate, the activation energies of grain boundary conduction (about 1.3 eV) present values higher than that of the bulk: bulk conduction is associated with

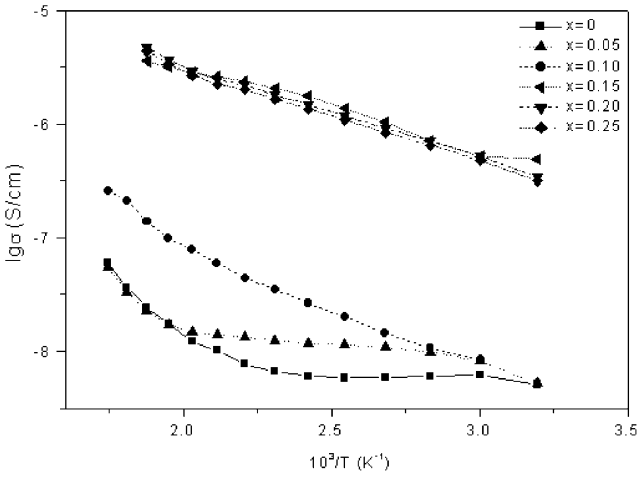

Fig. 7. Arrhenius plot of total conductivity of $Ce_{1-x}Nd_xO_{2-\delta}$ solid solutions, sintered at 1600°C, in the temperature range 40–400°C.

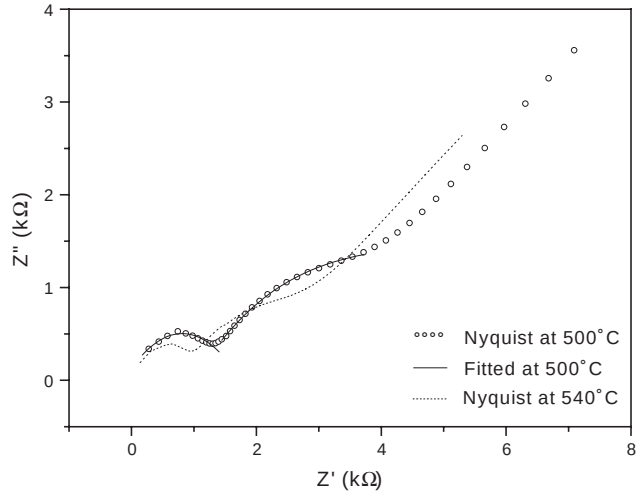

Fig. 8. Nyquist representations of impedances obtained at 500°C and 540°C for a $Ce_{0.8}Nd_{0.2}O_{2-\delta}$ sample sintered at 1600°C.

activation energies of 0.7–0.9 eV for substituted samples. In the case of pure ceria, the observed activation energy has an intermediate value of about 1.08 eV.

For bulk conduction of substituted samples, the lower activation energy can be easily interpreted in terms of increase in charge carriers (oxygen vacancy) associated with increase of Nd^{3+} doping (Nd'_{Ce} doping). However, it should be noted that no significant variation of bulk activation energy vs. x can be observed.

For grain boundary conduction, the higher activation energy can be interpreted first in terms of intrinsic character of inter-granular junctions, but also in terms of imperfect reaction occurring between the initial phases (Nd_2O_3, CeO_2), involving additional insulating interfaces in the material.

Finally, additional information has been obtained from the electrode conduction that presents activation energies ranging between 0.8 and 1.04 eV.

One interesting electrical characteristic reported in Table 2 is the exponent n of the electrical CPE model.

In the case of bulk behavior, this exponent n is close to 1. This is related to a homogeneous substituted phase.

In the case of grain boundary behavior, Fig. 10 shows the variation of the exponent n with temperature T. The n value is close to 0.5 up to 580–600°C, and then regularly increases to reach 0.9 at 700°C. It is interesting to note that such an exponent n does not clearly depend on the composition x.

In the case of electrode behavior, the exponent n is quasi-constant and close to 0.5.

Three types of capacitance values are observed in Table 2. For substituted samples, bulk capacitances are weak and increase as a function of temperature in the range 2×10^{-11}–40×10^{-11} F, grain boundary capacitances are higher (10^{-6} F) and vary in a non-linear way with an optimum occurring close to 580°C for some samples (Fig. 11). This evolution can be correlated with the change in n exponent above the same temperature. In the same substituted samples, the electrode capacitances regularly increase with several orders of magnitude of about 10^{-6} F.

4. Conclusions

When the three signals corresponding to bulk, grain boundaries (interfaces) and electrode (sample-metal interface) can be separately analyzed through Nyquist representations, the following major observations can be done:

- for increasing Nd compositions, bulk and grain boundary conductivities regularly increase, then, apparently, conductivity reaches a constant value in the range $x=0.10$–0.25;
- in substituted samples, activation energies do not clearly vary: however, the activation energies of grain core conduction are lower than those of grain boundaries;
- the various exponents n of the CPE electrical model seem to be significant factors for microstructure characterizations.

The observed evolutions of conduction with temperature and composition partly confirm previous literature results ([7–10]): for low Nd molar fractions, the increase in conductivity can be ascribed to the increasing formation of isolated defects (Nd and vacancies) or of isolated clusters Nd^{3+}–$[V_O^{\bullet\bullet}]$–Nd^{3+}. Above a certain Nd fraction, condensation of defects associated with percolation of charge carriers should occur. However, our results do not confirm any variation of activation

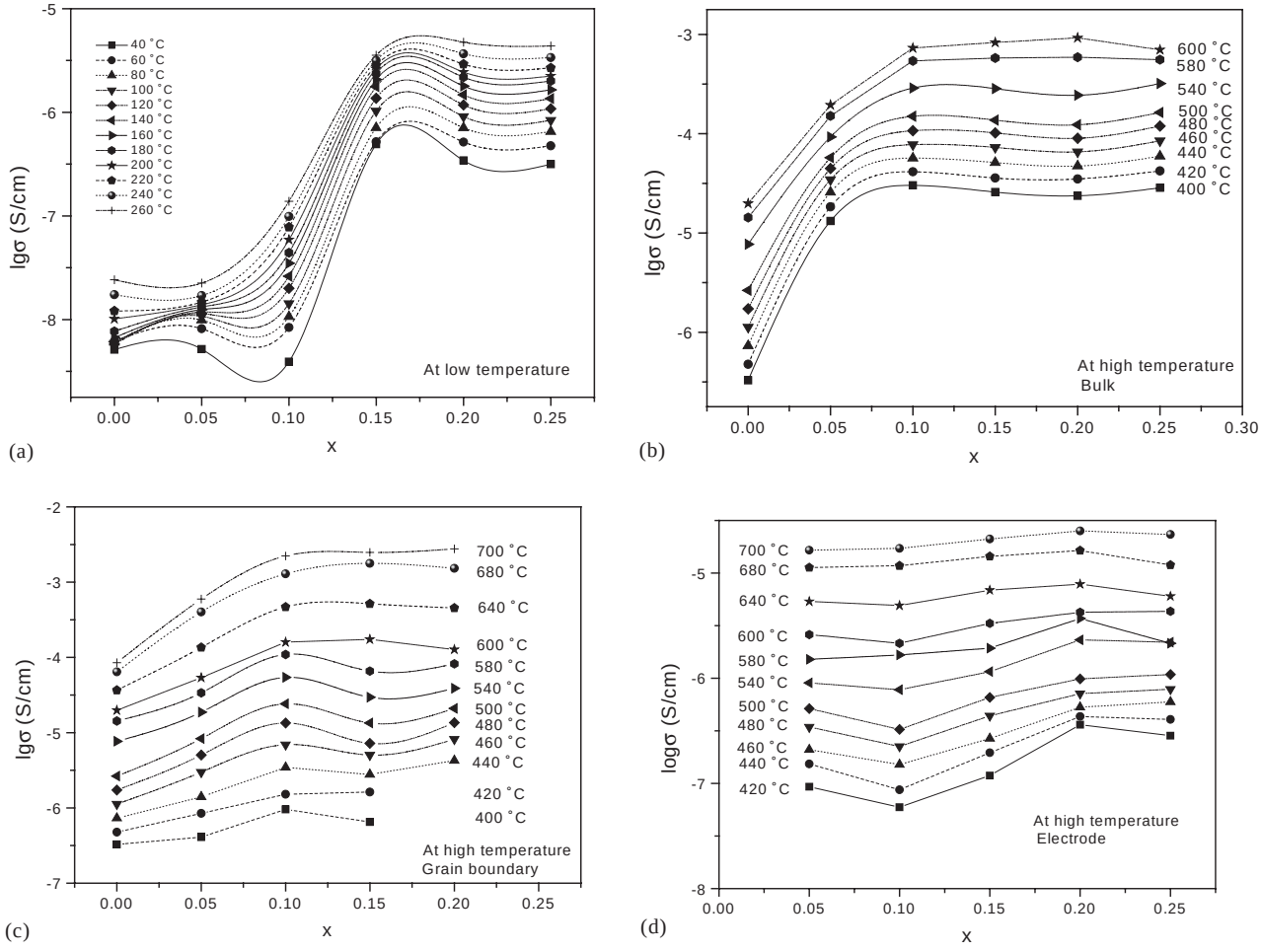

Fig. 9. Variation vs. x of the various conductivity contributions for $Ce_{1-x}Nd_xO_{2-\delta}$ solid solutions sintered at 1600°C: (a) unique component in the low-temperature range 40–400°C; (b) bulk component in the 400–700°C range; (c) grain boundary component in the 400–700°C range; and (d) electrode contribution in the 400–700°C range.

Table 3
Activation energy of $Ce_{1-x}Nd_xO_{2-\delta}$ solid solutions sintered at 1600°C

Component	Low temperatures (40–400°C) Total: E_a (eV) ± 0.05 eV	High temperatures (400–700°C)		
		E_a (bulk) ± 0.10 eV	E_a (grain boundaries) ± 0.10 eV	E_a (electrode) ± 0.10 eV
$CeO_{2-\delta}$	0.09	1.08 (total)	1.08 (total)	—
$Ce_{0.95}Nd_{0.05}O_{2-\delta}$	0.04	0.68	1.31	0.97
$Ce_{0.90}Nd_{0.10}O_{2-\delta}$	0.22	0.88	1.41	1.04
$Ce_{0.85}Nd_{0.15}O_{2-\delta}$	0.16	0.89	1.47	1.04
$Ce_{0.80}Nd_{0.20}O_{2-\delta}$	0.16	0.91	1.40	0.85
$Ce_{0.75}Nd_{0.25}O_{2-\delta}$	0.16	0.76	—	0.82

energies: it should be remarked that when the Nyquist signals can be separated, we obtain two activation energies showing two different migration mechanisms in grain core (resistance R_1) and grain boundaries (resistance R_2). If we had considered the sole variation of the total resistance ($R_1 + R_2$), we could have observed a certain composition dependence of activation energies: however, such an evolution should have artificially represented the behavior of hypothetical average ceramics.

The exponents "n", determined from CPE models, play an important role in the interpretation of conduction mechanisms, because they are well representative of the material microstructure. The obtained values of these exponents give pertinent informations. Grain cores are relatively homogeneous resistor–capacitor systems

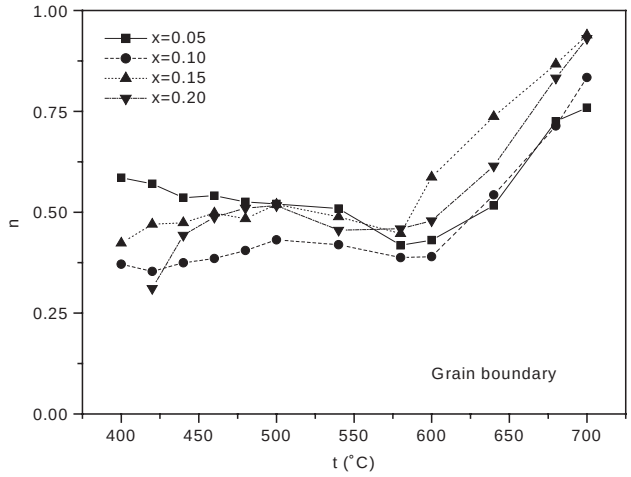

Fig. 10. Variation of the n exponent (CPE model) vs. temperature for grain boundary behavior.

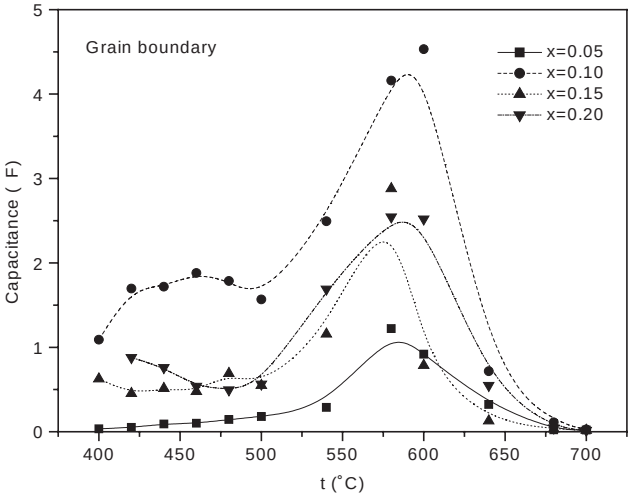

Fig. 11. Variation of capacitance vs. temperature for grain boundary contribution.

($n = 1$); grain boundaries are heterogeneous, with an abnormal evolution of n above 580°C; finally, electrode contribution is characterized by a porous character with $n = 0.5$ in the full temperature range. In the case of grain boundary contribution, the observed abnormal evolution with temperature of exponent n is not really understood: it might be correlated with a capacitance anomaly (broad peak of dielectric parameter). Such abnormal evolutions might be associated with a mechanical softening of interfaces, or an increasing contribution of oxygen conduction through these interfaces.

Finally, it should be remarked that the conduction behaviors (activation energies) strongly differ at low ($t < 400$°C) and high temperatures ($t > 400$°C). In both cases, at low or high temperature, the conduction reaches a maximum value above a limit of composition of about 10% Nd. It should be interesting to establish correlations between catalytic effects occurring in the low-temperature ranges and the conduction as a function of Nd composition. Catalytic studies with CH_4 and CO gas in air are now planned to try to connect catalytic efficiency with composition x, mainly close to the limit composition $x = 0.10$.

References

[1] H. Inaba, H. Tagawa, Solid State Ionics 83 (1996) 1.
[2] A. Trovarelli, Catal. Rev. Sci. Eng. 38 (1996) 439.
[3] P.J. Gellings, H.I.-M. Bouwmeester, Catal. Today 1 (1992) 1.
[4] Y. Teraoka, H.M. Zhang, S. Furukawa, N. Yamazoe, N. Chem. Lett. N 10 (1985) 1743.
[5] C.R.A. Catlow, Solid State Ionics 36 (1989) 71.
[6] W. Huang, P. Shuk, M. Greenblatt, Chem. Mater. 9 (1997) 2240.
[7] C.J. Kevane, E.L. Holverson, R.D. Watson, J. Appl. Phys. 34 (1963) 2083.
[8] T. Kudo, H. Obayashi, J. Electrochem. Soc. 122 (1975) 142.
[9] T. Kudo, H. Obayashi, J. Electrochem. Soc. 123 (1976) 415.
[10] R.T. Dirstine, R.N. Blumenthal, T.F. Kuech, J. Electrochem. Soc. 126 (1979) 264.
[11] D.K. Hohnke, Solid State Ionics 5 (1981) 531.
[12] H. Yahiro, Y. Eguchi, K. Eguchi, H. Arai, J. Appl. Electrochem. 18 (1988) 527.
[13] H. Yahiro, K. Eguchi, H. Arai, Solid State Ionics 36 (1989) 71.
[14] I. Riess, D. Braunshtein, D.S. Tannhauser, J. Am. Ceram. Soc. 64 (1981) 479.
[15] D.Y. Wang, A.S. Nowick, J. Solid State Chem. 35 (1980) 325.
[16] J. Faber, C. Geoffroy, A. Roux, A. Sylvestre, P. Abélard, Appl. Phys. A 49 (1989) 225.
[17] K. Huang, M. Feng, J.B. Goodenough, J. Am. Ceram. Soc. 81 (1998) 357.
[18] J.A. Kilner, J.D. Faktor, in: T.A. Wheat, A.K. Kuriakose (Eds.), Progress in Solid Electrolytes, Publication ERP/MSL 83–94 (TR), Energy, Mines and Resources, Ottawa, Canada, 1983, p. 347.
[19] S. Villain, Ch. Leroux, J. Musso, J.R. Gavarri, A. Kopia, M. Klimczak, J. Kusinski, J. Metast. Nano. Mater. 12 (2002) 59.
[20] T. Roisnel, J.R. Carvajal, Winplotr, version June 2001 (LLB-LCSIM).
[21] R.D. Shannon, C.T. Prewitt, Acta Crystallogr. A 32 (1976) 751.
[22] J.E. Bauerle, J. Phys. Chem. Solids 30 (1969) 2657.
[23] C.S. Hsu, F. Mansfeld, Corrosion 57 (2001) 747.
[24] W.H. Mulder, J.H. Sluyters, T. Pajkossy, L. Nyikos, J. Electroanal. Chem. 285 (1990) 103.
[25] J.R. Macdonald (Ed.), Impedance Spectroscopy, Wiley, New York, 1987 (ISBN 0-471-83122-0).
[26] B.C.H. Steele, in: T. Takahashi (Ed.), High Conductivity Solid Ionic Conductors, Recent Trends and Applications, World Scientific, Singapore, 1989, p. 402.
[27] S.P.S. Badwal, Mater. Sci. Technol.: A Comprehensive Treatment 11 (1994) 567.